CDF Hot Topics

S. Donati
University of Pisa, Pisa, Italy

In this paper we review the most recent CDF results in the fields of b and c Physics.

1. Introduction

B hadrons are abundantly produced at the Tevatron Collider, the measured B^+ cross section is 2.78 ± 0.24 μb in the region of transverse momentum $p_T(B^+) > 6.0$ GeV/c and rapidity $\mid y(B^+) \mid < 1$ [1]. This cross section is three orders of magnitude larger than at e^+e^- machines running at the $\Upsilon(4S)$ and the available energy allows the production of the heavier B_s^0, B_c and Λ_b hadrons. The challenge is extracting the interesting B signals from a level of background which is three orders of magnitude higher at production. This is achieved at CDF II with dedicated detectors and triggers. The current CDF hot topics reviewed in this paper are the recent analysis which sets the first bound on the mixing induced CP violation in the $B_s^0 \to J/\psi\phi$ decays, the analysis leading to the world best limits on the $B_s^0 \to \mu^+\mu^-$ branching fraction, the B_c and B_s^0 lifetime measurements, the analysis leading to the evidence for the D^0 mixing and the search for the $D^0 \to \mu^+\mu^-$ decay.

2. The Tevatron Collider and the CDF II Detector

The Tevatron Collider collides 36 $p\overline{p}$ bunches at $\sqrt{s} = 1.96$ TeV. The design instantaneous luminosity was 10^{32} cm^{-2}s^{-1} but the Tevatron largely exceeded it and set the peak luminosity record above 3.0×10^{32} cm^{-2}s^{-1}. With an already integrated luminosity larger than 3.2 fb^{-1}, the expectation is to have integrated $\sim$6 fb^{-1} by the year 2010.

2.1. Tracking Detectors

The CDF II tracker is located within a 14.1 kG solenoidal magnetic field and it is composed of silicon detectors and a drift chamber. There are three independent silicon detectors, SVXII, ISL and L00, for a total of eight silicon layers, 704 ladders and 722,432 channels [2]. SVXII is made of 360 double-sided ladders in a layout of six 15 cm axial sections $\times$ twelve 30° ϕ slices $\times$ five radial layers between 2.5 and 10.6 cm from the beamline. ISL covers the area between SVXII and the drift chamber, with 296 double-sided ladders at radii of 20 and 28 cm. With a length of 1.9 m, it provides silicon hits out to $\mid \eta \mid < 2$. L00 is a single-sided layer of 48 ladders mounted directly on the beampipe, 1.5 cm from the beamline, which enhances the track impact parameter resolution. The three subdetectors share the same readout system, starting with the SVX3D chip, a custom designed ASIC with a 128 channel $\times$ 42 capacitor analog storage ring, which makes it possible to acquire data in deadtimeless mode, integrating charge on one capacitor while reading out another one. The data acquisition system provides silicon data in time for Level 2 trigger processing. Over 90 % of the silicon detector is powered and more than 80 % is providing quality data. Charge collection efficiency is 99 % , with a single hit efficiency > 90 %. The hit resolution for a two-strip cluster is 9 μm. The signal-to-noise ratio is above 10:1 both for $r-\phi$ strips and for $r-z$ strips. The Central Outer Chamber (COT, [3]) is located outside the silicon detectors and inside the time-of-flight detector scintillators. The active volume of the COT spans 310 cm in the beam direction, 43.4 cm and 132.3 cm in radius, and the entire azimuth. The COT contains 30,240 sense wires that run the length of the chamber between two end plates. Approximately half of the wires are axial (run along the z direction) and half are small angle (2°) stereo. The $r-\phi$ view provides information for the p_T measurement, the $r-z$ view for the η measurement. The COT contains 96 sense wire layers in radius that are grouped into eight superlayers. Each superlayer is divided into supercells along the azimuthal angle, and each supercell has 12 sense wires and a maximum drift distance that is approximately the same for all superlayers. Therefore the number of supercells in a given superlayer scales approximately with the radius of the superlayer. The supercell layout consists of a wire plane containing sense and potential (or field shaping) wires and a field (or cathode) sheet on either side. Each field sheet is shared with the neighboring cell. The supercell is tilted by 35° with respect to the radial direction to compensate for the Lorentz angle of the drifting electrons in the magnetic field. The gas is a mixture or Ar/Et (50:50) and Isopropyl which provides a maximum drift time of 177 ns on the maximum drift distance of 0.88 cm. The measurement of the pulse widths provides a measurement of the dE/dx in the chamber, used for particle identification. The achieved performance of the integrated CDF II tracker is a transverse momentum resolution $\sigma(p_T)/p_T^2 = 0.15$ % (GeV/c)$^{-1}$ and an impact parameter resolution $\sigma(d) = 35$ μm @2 GeV/c. This

performance is sufficient for the B physics analyses.

2.2. Particle Identification Detectors

CDF II uses two detectors and two complementary techniques for particle identification, one is the dE/dx measurement in the COT, the other one is the time-of-flight measurement in a dedicated detector. The COT readout electronics allows to measure the pulse width, which is related to the amount of charge collected by the wire. The truncated mean (80 %) computed on the hits associated to a track provides a measurement of the specific ionisation (dE/dx) in the chamber. A detailed calibration of the dE/dx measurement has been performed using samples of kaons and pions from $D^{*+} \rightarrow D^0\pi^+ \rightarrow [K^-\pi^+]\pi^+$, protons from $\Lambda^0 \rightarrow p\pi^-$, and muons and electrons from $J/\psi \rightarrow \mu^+\mu^-$ and $J/\psi \rightarrow e^+e^-$. The achieved K/π separation for $p_T > 2$ GeV/c is 1.4σ.

The Time-of-Flight detector (TOF, [4]) is installed between the drift chamber and the solenoid magnet and extends 4.7 cm radially at a radius of roughly 138 cm. The detector is composed by Bicron scintillator bars BC-408, selected for the long (2.5 m) attenuation length. The bars have a dimension of 4×4 cm^2 in cross-section and 279 cm in length. There are a total of 216 bars, each covering 1.7° in ϕ and $|\eta|<1$. The photomultipliers are attached to each end of every bar. The time resolution on the single hit is 110 ps and the K/π separation is better than 2σ for $p_T < 1.5$ GeV/c. By combining the dE/dx and the time-of-flight measurements, the achieved K/π separation is better than 1.4 σ in the entire momentum range.

2.3. Lepton Detectors

Segmented electromagnetic and hadronic calorimeters surround the tracking system [5]. The electron energy is measured by lead-scintillator sampling calorimeters. In the central region ($|\eta|<1.1$) the calorimeters are arranged in a projective barrel geometry and measure electromagnetic energy with a resolution of $|\sigma(E_T)/E_T|^2 = (13.5\ \%)^2/E_T(GeV) + (2\ \%)^2$. In the forward region ($1.2<|\eta|<3.5$) the calorimeters are arranged in a projective end-plug geometry and measure the electromagnetic energy with a resolution of $|\sigma(E_T)/E_T|^2 = (14.4\ \%)^2/E_T(GeV) + (0.7\ \%)^2$. Both central and forward electromagnetic calorimeters are instrumented with finely segmented detectors which measure the shower position at a depth where the energy deposition by a typical shower reaches its maximum. The central muon detector (CMU [6]) is located around the outside of the central hadron calorimeter at a radius of 347 cm from the beam axis. The calorimeter has a thickness of 5.5 interaction lengths and a ϕ segmentation of 15°. The muon drift cells are 226 cm long and cover 12.6° in ϕ, giving a ϕ coverage of 84 %. The pseudorapidity coverage is $|\eta| < 1$. Each module consists of four layers of four rectangular drift cells. The sense wires in alternating layers are offset by 2 mm for ambiguity resolution. The smallest unit in the CMU, called a stack, covers about 1.2° and includes four drift cells, one from each layer. Adjacent pairs of stacks are combined together to form a two-stack unit called a tower. A track segment detected in these chambers is called a CMU stub. A second set of muon chambers is located behind an additional 60 cm of steel. The chambers are arranged axially to form a box around the central detector. The coverage of the central muon system is extended to the region $0.6<|\eta|<1.0$ by four free-standing conical arches which hold drift chambers which cover 71 % of the solid angle.

2.4. Trigger and Data Acquisition

CDF II uses a three-level system to reduce the 1.7 MHz bunch crossing rate to 100 Hz written on tape. The Level 1 is a deadtimeless 7.6 MHz synchronous pipeline with 42 cells, which allows 5.5 μs to form a trigger decision. The maximum sustainable Level 1 output rate is ≈30 kHz. The Level 2 is an asynchronous pipeline with an average latency of 20 μs. While the events accepted by Level 1 are being processed by Level 2 processors, they are also stored on one of the four Level 2 buffers, waiting for the Level 2 trigger decision. Each buffer is emptied when the Level 2 decision for the corresponding event has been asserted: if the event has been accepted, the buffer is read out, else it is simply cleared. If the Level 2 trigger decision takes too much time and the four buffers are all filled, the Level 1 accept is inhibited. This is a source of deadtime for the CDF II trigger. The maximum Level 2 output rate is 300 Hz. The Level 3 trigger is made of a CPU farm and has a maximum output rate of 100 Hz.

The heart of the Level 1 trigger is the eXtremely Fast Tracker (XFT, [7] [8]), the trigger track processor that identifies high transverse momentum ($p_T >$ 1.5 GeV/c) charged tracks in the COT. The XFT tracks are three-dimensional and are extrapolated to the calorimeter and to the muon chambers to generate electron and muon trigger candidates. Track identification in the XFT is accomplished in two processes by the Finders and by the Linkers. The Finders search for track segments in the axial and stereo superlayers of the chamber. The Linkers search for matches among segments in the superlayers, consistent with prompt high-p_T tracks. The efficiency for finding XFT tracks is ≈90 %, with a transverse momentum resolution better than 2 % per GeV/c and azimuthal angular resolution of 5.5 mr. The level of fake tracks shows some growth with instantaneous luminosity.

The Online Silicon Vertex Tracker (SVT, [9]) is part

of the Level 2 trigger. It receives the list of XFT tracks and the digitised pulse heights on the axial layers of the silicon vertex detector. The SVT links the XFT tracks to the silicon hits and reconstructs tracks with offline-like quality. In particular the resolution on the impact parameter, which is a crucial parameter to select B events since they tipically show secondary vertices, is 35 μm for 2 GeV/c tracks. The SVT efficiency is 85 % per track. Since a long Level 2 processing time can introduce dead time, to speed up operations the SVT has a widely parallelized design: it is made of 12 identical azimuthal slices working in parallel. Each slice receives and processes data only from one silicon vertex detector 30° sector. In addition SVT recontructs only tracks in the transverse plane to the beamline and only with $p_T > 2.0$ GeV/c. The tracking process is performed in two steps. The first step is the pattern recognition: candidate tracks are searched among a list of precalculated low resolution patterns. This is done in order to reduce the huge amount of silicon hits only to those potentially interesting. The second step is track fitting: a full resolution fit of the hit coordinates found within each pattern is performed using a linearized algorithm. By providing a precision measurement of the impact parameter of the charged particle tracks, SVT allows triggering on events cointaining long lived particles, like the B events, which at the Tevatron have decay lengths of the order of 500 μm and produce tracks in the decay with impact parameters on average larger than 100 μm.

Level 3 trigger is implemented on a CPU farm which allows to perform an almost offline-quality event reconstruction.

2.5. Triggers for B physics

CDF II has basically three families of triggers for B physics: the dimuon trigger, the semileptonic trigger and the hadronic trigger.

The dimuon trigger selects muon pairs with transverse momenum as low as 1.5 GeV/c. It is mostly used to select J/ψs and $\psi(2S)$, to reconstruct the many decay modes of the B hadrons (B^0, B^+, B_s^0, B_c, and Λ_b) containing a J/ψ decaying to muon pairs, and to select $\Upsilon \to \mu^+\mu^-$ decays, or muon pairs for the search of the rare $B \to \mu^+\mu^- X$ decays, or for $b\overline{b}$ correlation studies.

The semileptonic trigger selects events with a lepton (μ or e) with $p_T > 4$ GeV/c and an SVT track with $p_T > 2$ GeV/c and impact parameter above 120 μm.

The hadronic trigger selects hadronic decay modes as $B^0_{(s)} \to h^+h^{'-}$ and $B_s^0 \to D_s^-\pi^+$. Te trigger requires track pairs with $p_T > 2$ GeV/c and $p_{T1} + p_{T2} > 5.5$ GeV/c, with an opening angle in the transverse plane below 135°, impact parameter above 100 μm, a decay length above 200 μm. For the two-body decay trigger path, optimised to collect $B \to h^+h^{'-}$ decays, the track pair is requested to point back to the primary vertex, by requiring that the impact parameter of the reconstructed B is below 140 μm. To select hadronic multibody decays, like $B_s^0 \to D_s^-\pi^+$, the request on the pointing back to the primary vertex has low efficiency, since the track pair provides only a partial reconstruction of the multibody decay, and it is not applied.

The Tevatron performance has been continuosly improving since the beginning of Run II. The high initial luminosity and the drop along the store require continuous monitoring and adjustments of the trigger strategy in order to have all the available bandwidth efficiently used at all luminosities. This has been achieved by implementing more versions of the same trigger with increasingly tighter cuts, and consequently increasing purity, and running the versions with tighter cuts with no prescale and the versions with looser cuts with a prescale. For the hadronic trigger the tighter version requires track pairs with $p_T > 2.5$ GeV/c and $p_{T1} + p_{T2} > 6.5$ GeV/c. The prescales can be made dynamical, and they adjust themselves as the luminosity decreases and more bandwidth becomes available. In addition to this, triggers are luminosity enabled: if the rate of a trigger that is important to keep unprescaled is too large at the initial luminosity, it is enabled only when the luminosity has decreased below a safe threshold.

3. First Bounds on Mixing-Induced CP Violation in $B_s^0 \to J/\psi\phi$ Decays

CDF has performed a first study of the $B_s^0 \to J/\psi\phi$ decay in which the initial state is identified as B_s^0, or its antiparticle $\overline{B}_s^0$ by using the process of flavor tagging. This information is used to separate the time evolution of mesons produced as B_s^0 or $\overline{B}_s^0$. By relating this time development with the CP eigenvalue of the final state that is accessible through the angular distribution of the J/ψ and ϕ mesons, we obtain direct sensitivity to the CP-violating phase. This phase enters the time development with terms proportional to both $|\cos(2\beta_s)|$ and $\sin(2\beta_s)$. Analyses of $B_s^0 \to J/\psi\phi$ decays that do not use flavor tagging provide information on $\Delta\Gamma$, and are primarily sensitive to $|\cos(2\beta_s)|$ and $|\sin(2\beta_s)|$, leading to a fourfold ambiguitiy in the determination of $2\beta_s$ [11][12]. This analysis uses 1.35 fb^{-1} of data collected by the dimuon trigger, which selects events containing $J/\psi \to \mu^+\mu^-$ decays. The $B_s^0 \to J/\psi\phi$ decays are reconstructed from the decays $J/\psi \to \mu^+\mu^-$ and $\phi \to K^+K^-$ and require these final states to originate from a common vertex. An artificial neural network is used to achieve optimal separation of signal from background [13]. The neural network uses particle identification information from the time-of-flight detector and the specific ionization

loss in the drift chamber, the transverse momentum components of the B_s^0 and ϕ candidates and the quality of the fit to the trajectories of the final state particles. For the network training MonteCarlo events are used as signal, while background events are from the B_s^0 mass sidebands in real data. The analysis uses the orbital angular momenta of the vector mesons produced in the decay of a pseudoscalr meson to distinguish between the CP-even (S- and D-wave) from the CP-odd (P-wave) final states. To separate the time development of the B_s^0 and $\overline{B}_s^0$, the flavor at the time of production is identified by means of two independent types of flavor tagging. The first type, known as opposite-side flavor tag, uses the decay products of the other b quark in the event, and is mainly based on the charge of the muons or electrons form the semileptonic B decays [14]. The second type correlates the flavor of the meson with the charge of an associated kaon, referred as same-side kaon, arising from fragmentation processes [15]. The parameters of interest, $2\beta_s$ and $\Delta\Gamma$, plus several additional parameters, including the mean B_s^0 width Γ, the mixing frequency Δm_s and the magnitudes of the polarisation amplitudes and the strong phases, are extracted from an unbinned maximum likelihood fit. The fit uses the B_s^0 candidate mass m and its undertainty σ_m (Figure 1), the B_s^0 proper decay time t and its uncertainty σ_t, the transversity angles [11], and the tag information. A confidence region in the $2\beta_s$-$\Delta\Gamma$ plane is constructed using the Feldman-Cousins methods [16], reported in Figure 2. Assuming the standard model predicted values of $2\beta_s = 0.04$ and $\Delta\Gamma = 0.096$ ps^{-1}, the probability of a deviation as large as the level observed in data is 15 % (1.5σ). If $\Delta\Gamma$ is treated as a nuisance parameter, and only $2\beta_s$ is determined from the fit, $2\beta_s$ falls in the window [0.32,2.82] at the 68 % confidence level. The new bounds restrict the knowledge of $2\beta_s$ to two of the four solutions allowed in the measurements that do not use flavor tagging [11][12].

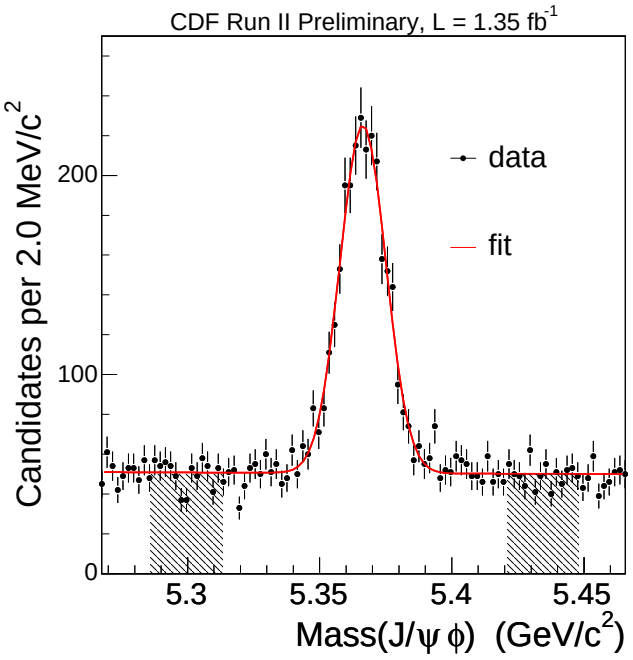

Figure 1: invariant $\mu^+\mu^- K^+K^-$ mass distribution with the fit projection overlaid.

4. Search for the $B_{(s)}^0 \to \mu^+\mu^-$ rare Decay

The FCNC decays $B_s^0(B^0) \to \mu^+\mu^-$ occur in the standard model only through higher order diagrams. The expectations for the branching fractions are $BR(B_s^0 \to \mu^+\mu^-) = (2.42 \pm 0.54) \times 10^{-9}$ and $BR(B^0 \to \mu^+\mu^-) = (1.0 \pm 0.14) \times 10^{-10}$ [17] which are one order of magnitude smaller than the current experimental sensitivity. In SUSY models diagrams including sypersymmetric particles can increase these branching fractions at large $tan(\beta)$ [18], and also at small $tan(\beta)$ [19]. The new measurement uses 2 fb^{-2} and the sensitivity is further improved by using an enhanced muon selection, and performing the search in a two dimensional grid in dimuon mass and neural network space. The discriminating variables used in the analysis include the measured proper decay time, λ, the proper decay time divided by the estimated uncertainty, λ/σ_λ, the 3D opening angle between the dimuon momentun and the displacement vector between the primary vertex and the dimuon vertex, $\Delta\Theta$, and the B-candidate track isolation, $I(B)$. To enhance signal and background separation a neural network discriminant is constructed, using all the discriminating variables except $m_{\mu\mu}$. The network is trained using MonteCarlo simulated $B_{(s)}^0$ events for signal and mass sidebands events for background. The mass search regions are $5.310 < m_{\mu\mu} < 5.430$ GeV/c^2 for the B_s^0 and $5.219 < m_{\mu\mu} < 5.339$ GeV/c^2 for the B^0, which approximately correspond to $\pm 2.5\sigma_m$ ($\sigma_m = 24$ MeV/c^2). The $B_s^0 \to \mu^+\mu^-$ branching fraction is determined relative to the $B^+ \to J/\psi K^+$ signal. Relative geometric acceptances and analysis efficiencies are estimated using MonteCarlo. The expected background is due to the contributions of the combinatorial continuum and from the $B_{(s)}^0 \to h^+h'^-$ decays.The contribution from the combinatorial is estimated by linearly extrapolating from the sideband region to the signal region. The contribution from $B_{(s)}^0 \to h^+h'^-$ decays is estimated to be one order of magnitude smaller than the conbinatorial background. Using an a priori optimization procedure, it was found that subdividing the signal region into several bins in mass and in the neural network variable improves the sensitivity of the analysis relative to using a single bin. The backgrounds, efficiencies and limits are computed in each bin separately. Figure 3 shows the $\mu^+\mu^-$

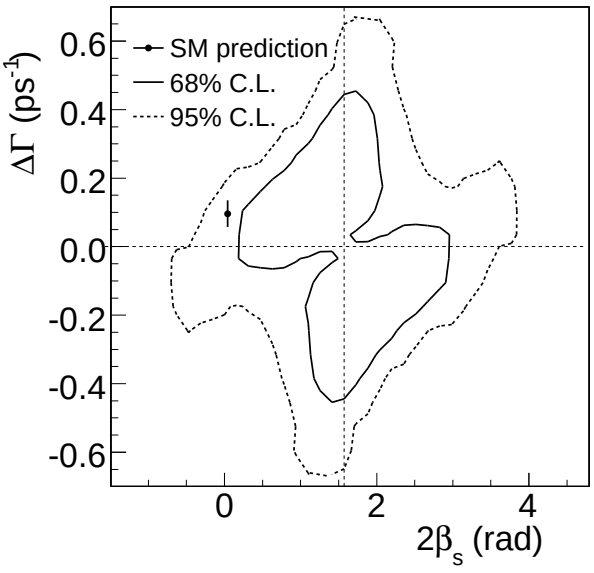

Figure 2: Feldman-Cousins confidence region in the $2\beta_s - \Delta\Gamma$ plane, where the standard model favored point is shown with error bars. The intersection of the horizontal and vertical dotted lines indicates the reflection symmetry in the $2\beta_s$ - $\Delta\Gamma$ plane.

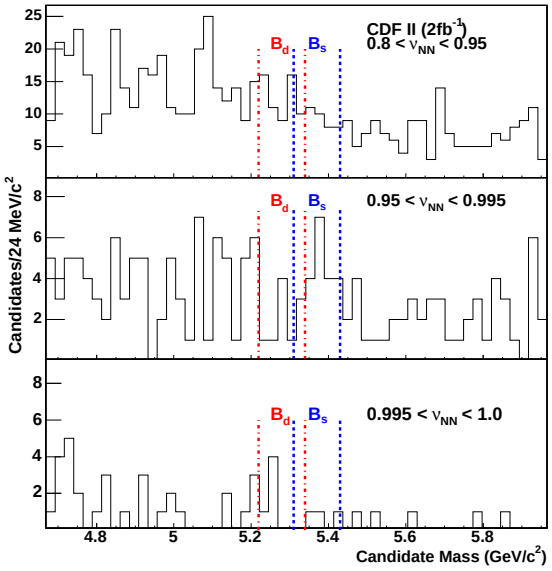

Figure 3: The $\mu^+\mu^-$ invariant mass distribution for events satisfying all selection criteria for the final three ranges of the neural network variable.

mass distribution for three different ranges of the neural network variable. We extract the following limits $BR(B_s^0 \to \mu^+\mu^-) < 5.8(4.7) \times 10^{-8}$ at 95(90) % C.L. and $BR(B^0 \to \mu^+\mu^-) < 1.8(1.5) \times 10^{-8}$ at 95(90) % C.L., which place further constraints on new-physics models [18][19].

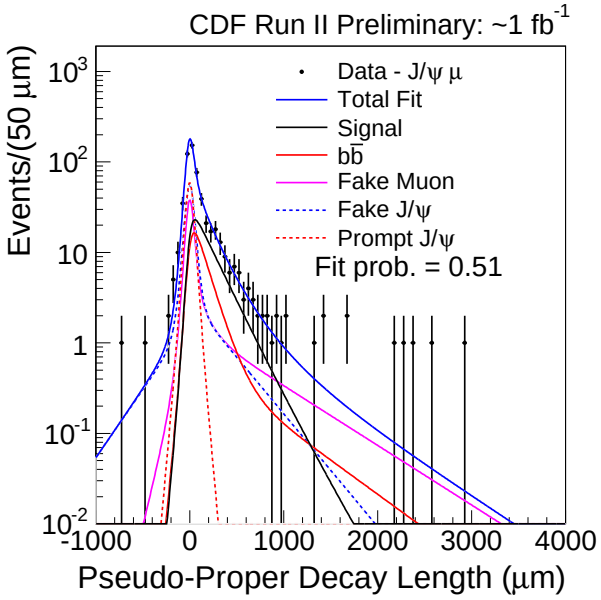

Figure 4: Fitted ct^* for the $J/\psi\mu$ candidate events, where background are shown broken into individual components.

5. New B_c and B_s^0 Lifetime Measurements

CDF has measured the B_c^+ lifetime in 1 fb^{-1} of inclusive $J/\psi \to \mu^+\mu^-$ data using the $B^\pm \to J/\psi l^\pm X$ decays, where l can be an electron or a muon and X are unmeasured particles. To measure the lifetime, we reconstruct a per event lifetime defined using variables measured in the transverse plane. Since not all the decay products of the B_c decay are identified, we define a

$$ct^* = \frac{mL_{xy}(J/\psi l)}{p_T(J/\psi l)} \qquad (1)$$

from which we can obtain the true B_c lifetime by defining a factor K, determined using MonteCarlo, where $ct = Kct^*$. The B_c signal is reconstructed by selecting dimuon events with a di-muon mass falling within ± 50 MeV/c^2 window around the J/ψ mass, and requiring the presence of a third lepton forming a vertex with the J/ψ candidate. Most B_c signal is expected in the window with $4.0 < m_{J/\psi l} < 6.0$ GeV/c^2. The broad mass peak includes also significant amount of background, mainly due to events with a J/ψ from $b\bar{b}$ and $c\bar{c}$ and an additional hadron which fakes a muon by punching through to the muon chambers, or an electron by leaving a signature in the calorimeter compatible with an electron, to events from the continuum background for J/ψ with a third lepton, to $b\bar{b}$ events with a J/ψ froma b-quark jet and a lepton from the other b, or events where conversions produce electrons which produce a B_c candidate when paired to a J/ψ. Each of these background sources

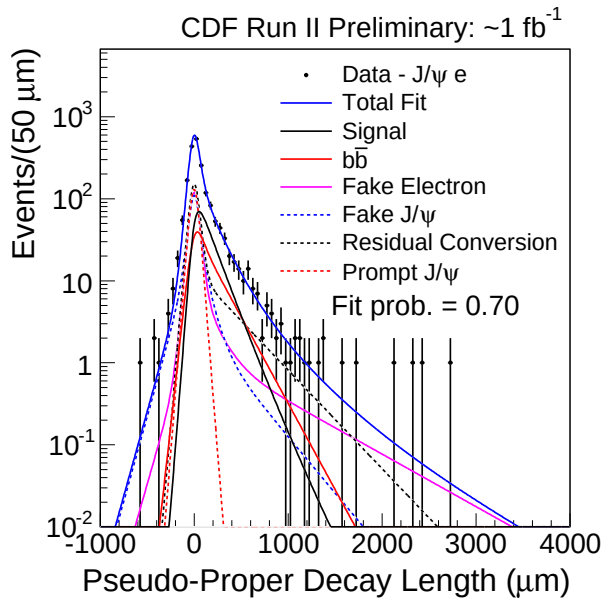

Figure 5: Fitted ct^* for the $J/\psi e$ candidate events, where background are shown broken into individual components.

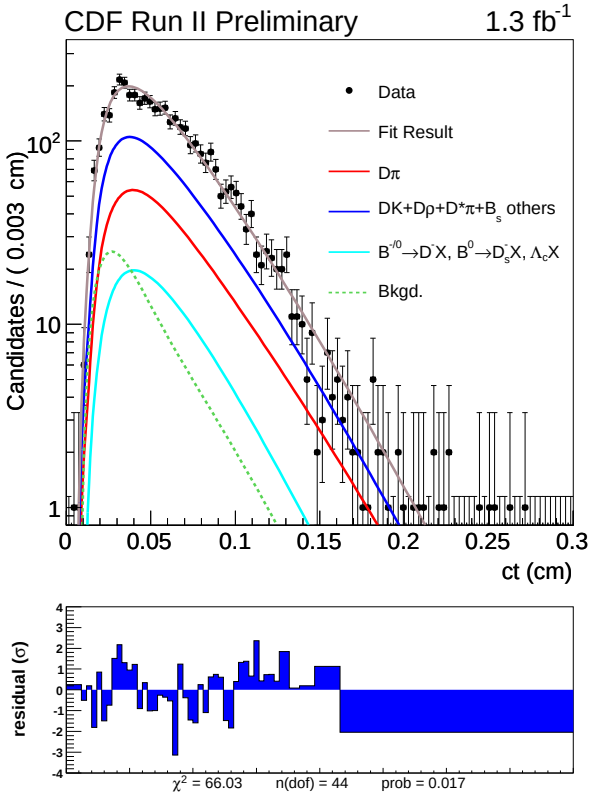

Figure 6: ct projection of the lifetime fit for events reconstructed as $B_s^0 \to D_s^-(\phi\pi^-)\pi^+$.

are estimated by using control samples and simulation. The fit of the ct^* distributions is performed separately in the $J/\psi l$ and $J/\psi e$ decay modes, using likelihood functions (Figure 4 and 5). The combined result is $c\tau = 142.5^{+15.8}_{-14.8}(stat.) \pm 5.5(syst.)$ μm, where the largest contributions to the systematic error is due to the resolution function and to the uncertainty on the silicon alignment.

A new CDF analysis has measured the B_s^0 lifetime using 1.3 fb^{-1} of data reconstructed as $B_s^0 \to D_s^-(\phi\pi^-)\pi^+$ and $B_s^0 \to D_s^-(\phi\pi^-)\rho^+(\pi^+\pi^0)$, where the π^0 is not reconstructed. The analysis reconstructs about 1100 fully reconstructed $B_s^0 \to D_s^-(\phi\pi^-)\pi^+$ candidates and a similar number of partially reconstructed $B_s^0 \to D_s^-(\phi\pi^-)\rho^+(\pi^+\pi^0)$ decays. The increased statistics has an uncertainty due to the missing tracks or misassigned masses, but it can be properly accounted for and folded into the likelihood formulation. The lifetime fit of the B_s^0 meson is determined from two fits done sequentially. The first fit is of the reconstructed mass of the B_s^0 and it determines the relative fractions of the various decay modes and backgrounds. The second fit is of the proper decay time of the B_s^0 candidates and uses the fractions determined with the mass fit (Figure 6). The analisys determines $c\tau = 455.0 \pm 12.2(stat.) \pm 7.4(syst.)$, where the main systematics are due to the background model and to the uncertainty in the measurement of the fractions of the several contributions, to the uncertainty of the shape of the MonteCarlo $p_T(B_s^0)$ distribution and to the silicon detectors alignment.

6. CP Violation in the $B \to DK$ and $\Lambda_b^0 \to h^+h'^-$ decays

CDF has also performed analyses in the field of CP violation using hadronic decays reconstructed in 1 fb^{-1} of data. A first analysis uses the $B^- \to D^0K^-$ modes, which allow a theoretically-clean extraction of the CKM angle γ by a variety of methods, depending on the involved specific D^0 decay mode [20][21][22][23]. These methods require no flavor tagging or time-dependent measurements and use only charged particles in the final state, which makes them well suited for a hadron collider environment. By using the data collected by the hadronic trigger we have reconstructed the modes where the D^0 decays to either $K^-\pi^+$ (flavor eigenstate) or K^-K^+, $\pi^-\pi^+$ (CP-even eigenstate). The relevant modes are separated from the larger $B^- \to D^0\pi^-$ modes by using a likelihood fit which exploits the kinematic differences among the decay modes and the particle identification information provided by the specific ionization in the drift chamber. The most relevant result of this analysis is the first measurement at a hadron collider of the direct CP asymmetry in the $B^- \to D^0_{CP+}K^-$ decay mode, $A_{CP+} = 0.37 \pm 0.14(stat.) \pm 0.04(syst.)$, which is in good agreement with the measurements performed at

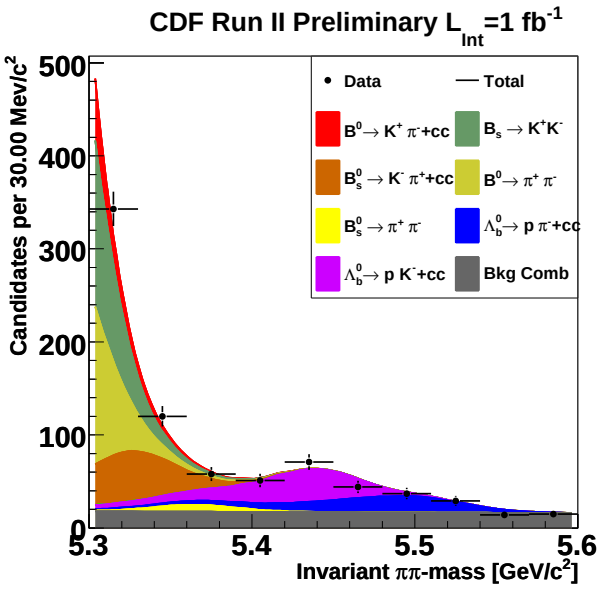

Figure 7: Invariant di-hadron mass distribution in the Λ_b^0 mass window with the result of the fit overlaid.

the $\Upsilon(4S)$ and has a comparable resolution. The analysis measures also other decay parameters useful to improve the determination of the CKM angle γ.

CDF has also performed a first measurement of CP-violating asymmetries and branching fractions of Λ_b^0 charmless two-body decays. These decays in a proton and a charged kaon or pion may show significant CP-violating asymmetries, of the order of 30 %. A measurement of these asymmetries may be useful to allow or rule out some extensions of the standard model [24][25]. The analysis uses the same general framework used for the measurement of two-body charmless decays of the B mesons, reported in [26]. An unbinned maximum likelihood fit, using kinematic information as well as particle identification information from the specific ionization measurement in the drift chamber, is used to measure the different components of the Λ_b^0 signal. These variables allow also to separate the Λ_b^0 from the $\overline{\Lambda}_b^0$ decays, thus allowing for a measurement of the direct CP asymmetry. The necessary corrections which take into account detector acceptance effects and trigger and offline selection efficiencies are determined from control samples and from simulated samples. Figure 7 reports the di-hadron mass distribution reconstructed in data in the Λ_b^0 window. We have measured $A_{CP}(\Lambda_b^0 \to p\pi^-) = 0.03 \pm 0.17(stat.) \pm 0.05(syst.)$ and $A_{CP}(\Lambda_b^0 \to pK^-) = 0.37 \pm 0.17(stat.) \pm 0.03(syst.)$

7. Evidence for D^0 Mixing and Search for the $D^0 \to \mu^+\mu^-$ rare Decay

The recent evidence for D^0 mixing has been found in two different types of measurements. The BELLE Collaboration found direct evidence of a longer and shorter lived D^0 meson [27], the BaBar Collaboration found a difference in decay time distribution for $D^0 \to K^+\pi^-$ compared to that for $D^0 \to K^-\pi^+$ [28]. CDF has performed a measurement comparing the decay time distribution for $D^0 \to K^+\pi^-$ compared to that for $D^0 \to K^-\pi^+$. The ratio $R(t)$ of $K^+\pi^-$ to $K^-\pi^+$ can be expressed as a simple quadratic function of proper time t under the assumption of CP conservation and small values for the parameters x and y [29], where the parameter x is defined in terms of the mass difference Δm between the heavy and light mass eigenstates and the parameter y involves the width difference $\Delta\Gamma$ between these states. The CDF measurement uses 1.5 fb^{-1} of data collected by the hadronic trigger. We reconstruct the Cabibbo-favored decay chain $D^{*+} \to D^0\pi^+$, with $D^0 \to K^-\pi^+$ called "right sign" and the corresponding "wrong sign" and the selection cuts are chosen as to maximise the significance of the wrong sign signal. The ratio of wrong sign to right sign D^* is determined by dividing the time distribution in bins. The distribution is fit to a parabola, related to the mixing parameters (Figure 8). The uncertainty on the mixing parameters includes effects from statistical fluctuations, uncertainties from the signal and background shapes and the corrections due to charm mesons from B decays. A Bayesian method is used to get the probability for different mixing parameters values. Contours containing the highest probability points are shown in Figure 9. The no-mixing point lies outside the contour equivalent to 3.8σ standard deviations, which is evidence of chamr mixing.

CDF has also searched for the rare $D^0 \to \mu^+\mu^-$ decay, which is suppressed by the GIM mechanism in the standard model which predicts a branching fraction of the order of 10^{-13} [30], with possible enhancements of seven orders of magnitude in R-parity violating SUSY models. The CDF anaysis has been performed with 360 pb^{-1} of hadronic data and follows the same strategy as in the previous CDF measurement [31]. The two-track candidates are reconstructed with the $\mu^+\mu^-$ mass hypothesis, and the D^{*-} tag mass-difference is applied to reduce the combinatorial background. By using the well known $D^0 \to \pi^+\pi^-$ decay mode as a normalisation mode, the analysis set the limit $BR(D^0 \to \mu^+\mu^-) < 0.43(0.53) \times 10^{-6}$ at the 90(95) % C.L.

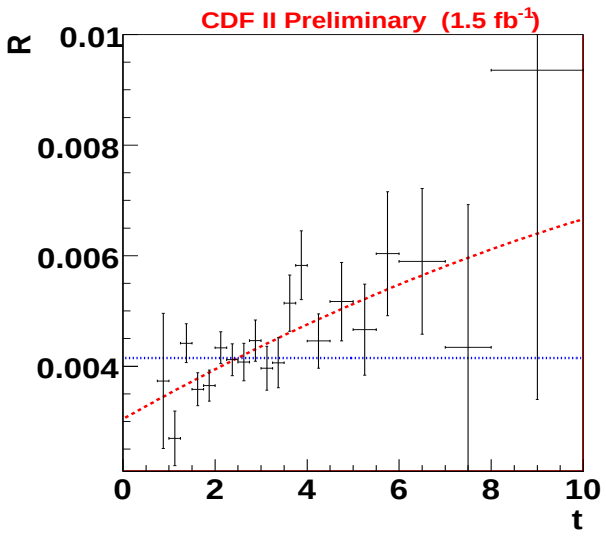

Figure 8: Ratio of the prompt D^* "wrong-sign" to "right-sign" decays as a function of normalized proper decay time. The dashed curve is from a least-squares quadratic fit. The mixing parameters are determined from this fit. The dotted line is the best fit if we assume no mixing.

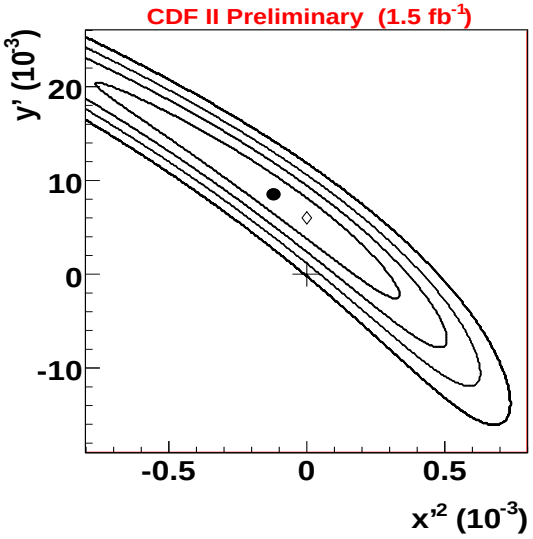

Figure 9: Bayesian probability countours in the parameter space corresponding to one through four equivalent Guassian standard deviations. The closed circle is the best fit value for the mixing parameters. The open diamond is the highest probability point that is physically allowed. The cross is the no-mixing point.

8. Conclusions

In this paper we have reviewed the current CDF hot topics in the fields of b and c physics. Most current CDF physics results are producd with 1-2 fb^{-1}. With the already collected 3.5 fb^{-1} and the total 6 fb^{-1} expected by the end of the year 2009, CDF expects to increase signficantly the number and the quality of the physics results in these sectors.

References

[1] D. Acosta et al., the CDF Collaboration, Phys. Rev. D 75, 012010 (2007).
[2] A. Sill et al., Nucl. Instrum. Meth. A530:1 (2004).
[3] T. Affolder et al., Nucl. Instrum. Meth. A526:249 (2004).
[4] D. Acosta et al., Nucl. Instrum. Meth. A518:605 (2004).
[5] L. Balka et al., Nucl. Instrum. Meth. A267:272 (1988). M. Alborw. et al., Nucl. Instrum. Meth. A453:84 (2000).
[6] G. Ascoli et al., Nucl. Instrum. Meth. A268:33 (1988).
[7] E. J. Thomson et al., IEEE Trans. on Nucl. Sc. vol. 49, n. 3 (2002).
[8] A. Abulencia *et al.*, IEEE Trans. Nucl. Sci. 55, 126-132 (2008).
[9] A. Bardi et al., Nucl. Instrum. Meth. A485:178 (2002).
[10] W. Ashmanskas *et al.*, Nucl. Instrum. Meth. A518: 532, (2004)
[11] T. Aaltonen *et al.* (CDF Collaboration), Phys. Rev. Lett. 100, 121803 (2008).
[12] V. M. Abazov *et al.* (D0 Collaboration), Phys. Rev. Lett. 98, 121801 (2007).
[13] A. Zell *et al.*, "SNNS, Stuttgart Neural Network Simulator, User Manual, Version 3.2" (University of Stuttgart, Stuttgart, Germany, 1994) (Computer Science Department, Report No. 6/94, 1994).
[14] A. Abulencia *at al.* (CDF Collaboration) Phys. Rev. Lett 97, 062003 (2006).
[15] A. Ali and F. Barreiro, Z. Phys. C 30, 635 (1986); M. Gronau, A. Nippe and J. L. Rosner, Phys. Rev. D 47, 1988 (1993); M. Gronau and J. L. Rosner, Phys Rev. D 49, 254 (1994).
[16] G. J. Feldman and R. D. Cousins, Phys. Rev. D 57, 3873 (1998).
[17] G. Buchalla and A. J. Buras, Nucl. Phys. B400, 225 (1993); A. J. Buras, Phys. Lett. B566, 115 (2003).
[18] S. R. Choudhury and N. Gaur, Phys. Lett. B 451, 86 (1999).
[19] R. Arnowitt *et al.*, Phys. Lett. B 538, 121 (2002).
[20] M. Gronau and D. Wyler, Phys. Lett. B 265, 172 (1991).
[21] M. Gronau and D. London, Phys. Lett. B 253, 483 (1990).
[22] A. Atwood, I. Dunietz and A. Soni, Phys. Rev. D

63, 036005 (2000).
[23] D. Atwood, I. Duniets and A. Soni, Phys. Rev. Lett. 78, 3257 (1997).
[24] R.Mohanta *et al.* Phys. Rev. D 63, 074001 (2001).
[25] R. Mohanta *et al.* Phys. Rev. D 63, 056006 (2001).
[26] A. Abulencia *et al.* Phys. Rev. Lett. 97, 211802 (2006).
[27] M. Staric *et al.* (BELLE Collaboration), Phys. Rev. Lett 98, 211803 (2007).
[28] B. Aubert *et al.* (BaBar Collaboration), Phys. Rev. Lett. 98, 211802 (2007).
[29] B. Aubert *et al.* (BaBar Collaboration), Phys, Rev. Lett. 91, 171801 (2003).
[30] G. Burdman *et al.*, arXiv:hep-ph/0112235 v2 (March 2002).
[31] A. Acosta *et al.*, Phys. Rev. D 68, 091101 (2003).